

Surrogate-Based Modeling of Cryogenic Turbulent Cavitating Flows

Chien-Chou Tseng

Department of Mechanical Engineering
University of Michigan, Ann Arbor, MI, USA

Wei Shyy

Department of Aerospace Engineering
University of Michigan, Ann Arbor, MI, USA

Abstract

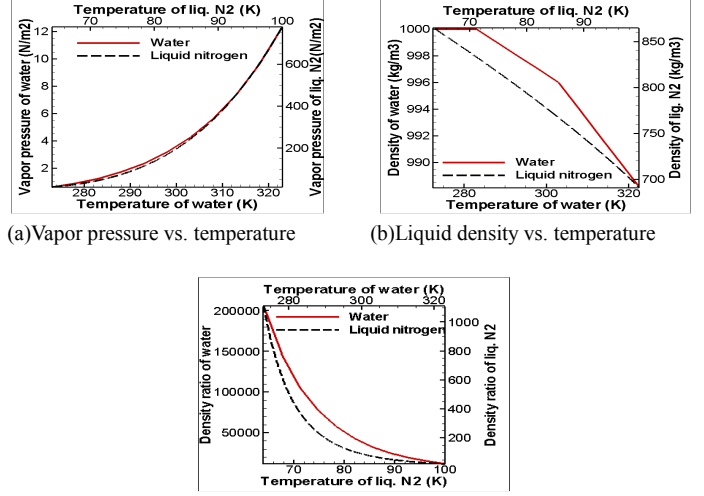
The cryogenic cavitation has critical implications on the performance and safety of liquid rocket engines. In this study, a systematic investigation based on the surrogate modeling techniques is conducted to assess and improve the performance of a transport-based cryogenic cavitation model. Based on the surrogate model, global sensitivity analysis is be conducted to assess the role of model parameters regulating the condensation and evaporation rates, and uncertainties in material properties, specifically, the vapor density and latent heat. The surrogate models considered include the response surface, radial basis neural network, Kriging, and a weighted average composite model combining all surrogates. It is revealed that the vapor density and the model parameter controlling the evaporation rate are more critical than latent heat and the model parameter controlling the condensation rate. Based on the recommended model parameter values, better prediction of the cryogenic turbulent cavitation can be attained.

1. Introduction

For the fuel delivery of liquid rockets, cavitation occurs as the local pressure is lower than vapor pressure, which can seriously compromise the engine performance and structural integrity [1,2]. At cryogenic conditions, the liquid/vapor density ratio is typically lower than that under non-cryogenic conditions. Thus, to sustain a comparable cavity size, heat transfer caused by latent heat becomes more important due to higher mass transfer rates. Consequently, the liquid surrounding the vapor cavity has more significant evaporative cooling in the cryogenic liquids. In addition, other transport properties such as thermal conductivity and thermodynamic properties such as vapor pressure of cryogenic fluid are very sensitive to temperature variations.

Substance	Heat capacity (J/Kg K)	Density ratio	Thermal conductivity (W/mK)	Latent heat (KJ/Kg)
H ₂ O(298k)	4200	43220	681	2442
N ₂ (83k)	2075	95	134	190
H ₂ (20k)	9484	57	103	446

Table 1. Variation of physical properties for water (298k), liquid nitrogen (83k), and liquid hydrogen (22k) on saturation curves. [5]



(a) Vapor pressure vs. temperature (b) Liquid density vs. temperature (c) Density ratio (liq./vapor) vs. temperature
(Solid lines represent for water and use bottom and left as x-axis and y-axis in each figure; dash lines represent for liquid nitrogen and use top and right as x-axis and y-axis in each figure)

Figure 1. Variation of physical properties for liquid nitrogen and water along saturation curve. [5]

Therefore, for cryogenic fluids, the energy transport equation needs to be included in the cavitation model [3,4]. Representative values of these quantities and the pressure-temperature saturation curves are summarized in Table 1 and Figure 1 [5].

The dynamic similarity for isothermal case, such as water is governed by the cavitation number [1,2,3]:

$$\sigma_{\infty} = (P_{\infty} - P_v) / 0.5 \rho_l U_{\infty}^2 \quad (1)$$

Where the cavitation number σ_{∞} is based on a constant vapor pressure P_v at inlet temperature T_{∞} . P_{∞} , ρ_l , and U_{∞} are reference pressure, liquid phase density and free stream velocity respectively. For cryogenic cavitation, the actual local cavitation number σ needs to be corrected according to the local temperature T :

$$\sigma = (P_{\infty} - P_v(T)) / 0.5 \rho_l U_{\infty}^2 \quad (2)$$

By the following first order approximation:

$$\frac{1}{2} \rho_l U_{\infty}^2 (\sigma - \sigma_{\infty}) = \frac{dp_v}{dT} (T_{\infty} - T) \quad (3)$$

$$\sigma = \sigma_{\infty} - \frac{dp_v}{dT} \frac{\Delta T}{0.5 \rho_l U_{\infty}^2}; \quad \Delta T = T - T_{\infty} < 0$$

Equation (3) clearly shows the temperature dependency of cavitation, and the local temperature drop in cryogenic cavitation will produce a noticeable rise for the local cavitation

number σ and hence suppress the cavitation intensity [3,4]. The detail impact for the thermal-sensible material properties to cavitation model will be introduced later.

The numerical modeling of cavitation largely follow two main categories: interface tracking methods with individual phases separately treated [6,7], and homogeneous flow models based on a single-fluid framework with fluid properties estimated based on the liquid-vapor mixture ratios [3,4,6,7,8,9,10,11,12,13,14,15]. Differences between the various models in the second category mostly come from the relation that defines the density field. For overview of the various modeling approaches, see, e.g., [3,4,8].

A homogeneous flow model utilizing the framework of the transport-based equation (TEM) is adopted in the present study. In this method, the information of the vapor volume/mass fraction distribution is obtained in a modeled transport equation based on the mass transfer between vapor and liquid phases. This approach is well documented, see, e.g., [3,4,8].

To study the impact of the cryogenic model parameters and fluid properties on the predictions, we conduct a model improvement exercise utilizing a global sensitivity analysis. We use the method developed by Sobol [16]. This method allows decomposition of a suitable measure of prediction into the components of individual variables from which we can easily calculate the impact of each variable. To facilitate the framework which helps us probe the global sensitivity of the cavitation model and fluid uncertainties, we will first construct suitable surrogate models [17].

The practical utility of surrogate modeling for design, optimization and sensitivity analysis is well established [18,19]. There are many surrogate models, but the model that represents a particular function the best is not known in advance. Then the predictions using different surrogate models have a certain amount of uncertainty. Goel et al [4,19] suggested that combinations of multiple surrogate models can be beneficial to quantify and to reduce uncertainties in predictions. They proposed a PRESS-based weighted average, namely PWS, (PRESS is the predicted residual sum of square) to reduce the model uncertainties.

Since the fidelity of surrogate models is critical in determining the success of the sensitivity analysis, we will use different surrogate models to help ascertain the performance measures. In this study, we use four surrogate models, polynomial response surface approximation (PRS, [20]), Kriging (KRG, [21]), radial basis neural network (RBNN, [22]) and PRESS-based weighted average (PWS) surrogate model constructed by using the previous three surrogates [4,17,19].

These surrogate models are used to calibrate the model parameters of the present transport based cavitation model for cryogenic cavitation. The surrogate-based global sensitivity analysis can help us investigate the uncertainties from fluid properties and then identify the optimal model parameters to improve the prediction performance and robustness of cryogenic cavitation models.

For turbulence closure, the ensemble-averaged modeling with a two-equation closure [23] along with a filter-based model (FBM) [24] is utilized. The approach reduces the influence of the turbulent eddy viscosity based on the local numerical resolution, essentially blending direct numerical

simulation (DNS) and conventional turbulence model in a single framework. Specifically, the level of the turbulent viscosity is corrected by comparing the turbulence length scale computed from the turbulence closure and the filter size Δ based on the local mesh spacing. This approach can be also categorized as Very Large Eddy Simulation (VLES) [25,26]. As documented in a previous study [27], the inlet conditions of the turbulence model can critically affect the outcome of cavitation structure. The filter-based model can help significantly reduce the uncertainty in this regard. In this study, we re-examine the surrogate-based cryogenic modeling efforts previously reported by Goel et al. [4] to assess the predictive capability of turbulent cavitating flows.

2. Governing Equations and Numerical Approaches

The set of governing equations for cryogenic cavitation under the homogeneous-fluid modeling consists of the conservative form of the Favre-averaged Navier-Stokes equations, the enthalpy-based energy equation (for cryogenic cavitation), the k- ϵ two-equation turbulence closure, and a transport equation for the liquid volume fraction [3,4,8]. The continuity, momentum, enthalpy, and cavitation model equations are given below. All computations presented below are based on the steady-state equations.

$$\frac{\partial(\rho_m u_j)}{\partial x_j} = 0 \quad (4)$$

$$\frac{\partial(\rho_m u_i u_j)}{\partial x_j} = -\frac{\partial p}{\partial x_i} + \frac{\partial}{\partial x_j} \left[(\mu_l + \mu_t) \left(\frac{\partial u_i}{\partial x_j} + \frac{\partial u_j}{\partial x_i} - \frac{2}{3} \frac{\partial u_k}{\partial x_k} \delta_{ij} \right) \right] \quad (5)$$

$$\frac{\partial}{\partial x_j} [\rho_m u_j (h + f_v L)] = \frac{\partial}{\partial x_j} \left[\left(\frac{\mu_m}{Pr_m} + \frac{\mu_t}{Pr_t} \right) \frac{\partial h}{\partial x_j} \right] \quad (6)$$

$$\frac{\partial(\alpha_l u_j)}{\partial x_j} = \dot{m}^+ + \dot{m}^- \quad (7)$$

where ρ_m is the mixture density, u_j denotes the components of velocity, p is the pressure, μ and μ_t are the mixture laminar and turbulent viscosities, respectively, h is the sensible enthalpy, f_v is the vapor mass fraction, L is the latent heat of vaporization, Pr is the Prandtl number, α_l is the liquid volume fraction, and \dot{m}^+ and \dot{m}^- are the source and sink terms for the cavitation model. The subscript 't' denotes turbulent properties, 'l' represents the liquid state, 'v' represents the vapor state, and 'm' denotes the mixture properties.

The mixture property ϕ_m and the vapor mass fraction are, respectively, expressed as

$$\phi_m = \phi_l \alpha_l + \phi_v (1 - \alpha_l) \quad (8)$$

$$f_v = \frac{\rho_v (1 - \alpha_l)}{\rho_m} \quad (9)$$

The temperature can be interpolated based on enthalpy in the data base [5]. We neglect the effects of kinetic energy and viscous dissipation terms in Equation (4) ($O(Re^{-0.5})$, Re is around 10^6) because the temperature field is mainly contributed by the evaporative cooling in cryogenic cavitation.

2.1. Transport-Based Cavitation Model

The source term m^+ and sink term m^- in Equation (7) represent for condensation and evaporation rates. They have been derived from various aspects, including dimensional argument with empirical support [3,4,8,10,11,12], force balance based on the interfacial dynamics [3,8,9], and estimate of the bubble growth rate through the Rayleigh-Plesset equation [13,14,15]. Numerically, [3,4,8,9,11,12] utilized pressure-based methods, and [10,12,16,13,14,15] employed the density-based methods. The liquid-vapor evaporation and condensation rates for the present transport-based cavitation model [3,4,8,10,11,12] are respectively shown as following:

$$\begin{aligned}\dot{m}^- &= \frac{C_{dest} \alpha_l \rho_l}{t_\infty \rho_v} \frac{\min(0, p - p_v)}{(0.5 \rho_l U_\infty^2)} \\ \dot{m}^+ &= \frac{C_{prod} (1 - \alpha_l)}{t_\infty} \frac{\max(0, p - p_v)}{(0.5 \rho_l U_\infty^2)}\end{aligned}\quad (10)$$

where C_{dest} and C_{prod} are the empirical constants, U_∞ is the reference velocity scale, and t_∞ is the reference time scale, which is the characteristic length scale D divided by the reference velocity scale U_∞ ($t_\infty = D/U_\infty$). For non-cryogenic fluids like water, the constants are specified $C_{dest} = 1$ and $C_{prod} = 80$ [3,8]. As for liquid nitrogen, the constants are chosen as $C_{dest} = 0.68$ and $C_{prod} = 54.4$, and for liquid hydrogen, $C_{dest} = 0.82$ and $C_{prod} = 54.4$ are suggested [3]. Further modifications are conducted to get a better prediction with $C_{dest} = 0.639$ and $C_{prod} = 54.4$ for liquid nitrogen, and $C_{dest} = 0.767$ and $C_{prod} = 54.4$ for liquid hydrogen [4]. For cryogenic cavitation simulations, the temperature dependent properties are updated from a comprehensive data base [5] throughout the course of computations for every iteration.

2.2. Thermodynamics Effects

The impact of thermal effects in cryogenic cavitation due to phase change on temperature prediction has been already shown in Figure 1. These thermo-sensible material properties will affect the energy equation in Equation (6) and cavitation sink/source terms in Equation (10).

First, the latent heat L in Equation (6) appears as a non-linear source term and represents the latent heat transfer rate during the phase change. The spatial variation of the thermodynamic properties together with the evaporative cooling effect is embedded into this equation and causes a coupling with the set of governing equations [3,4].

As for the cavitation sink/source terms in Equation (10), we can assess the impacts due to the thermo-sensible material properties by using Taylor's series and neglect the higher order terms. We first consider the sink term m^- as the pressure is smaller than the vapor pressure based on the local temperature [4,27], or in other words, pressure coefficient C_p is smaller than $-\sigma$. Furthermore, the minus sign here in Equation (11) is for convenience to show a larger evaporation strength will correspond to a larger positive value of m^- :

$$\begin{aligned}-\dot{m}^- &= -\frac{C_{dest} \alpha_l \rho_l}{t_\infty \rho_v} \left(\frac{\min(0, p - p_v(T))}{0.5 \rho_l U_\infty^2} \right) = -\beta R(T) \min(0, C_p + \sigma) \\ &= -\beta \left(R(T_\infty) + \frac{dR}{dT} \bigg|_{T_\infty} \Delta T + \dots \right) (C_p + \sigma_\infty - \frac{dp_v}{dT} \bigg|_{T_\infty} \frac{\Delta T}{0.5 \rho_l U_\infty^2} + \dots) \\ &= -\beta (R(T_\infty)(C_p + \sigma_\infty) + (C_p + \sigma_\infty) \frac{dR}{dT} \bigg|_{T_\infty} \Delta T - R(T_\infty) \frac{dp_v}{dT} \bigg|_{T_\infty} \frac{\Delta T}{0.5 \rho_l U_\infty^2} + \dots)\end{aligned}\quad (11)$$

where β is $C_{dest} \alpha_l / t_\infty$ and R is the temperature-dependent liquid/vapor density ratio. Similarly for source term m^+ as the pressure is larger than the vapor pressure (C_p is larger than $-\sigma$):

$$\begin{aligned}\dot{m}^+ &= \frac{C_{prod} (1 - \alpha_l)}{t_\infty} \frac{\max(0, p - p_v(T))}{0.5 \rho_l U_\infty^2} = \gamma \max(0, C_p + \sigma) \\ &= \gamma ((C_p + \sigma_\infty) - \frac{dp_v}{dT} \bigg|_{T_\infty} \frac{\Delta T}{0.5 \rho_l U_\infty^2} + \dots)\end{aligned}\quad (12)$$

Where γ is $C_{prod} (1 - \alpha_l) / t_\infty$. Please note that $\Delta T = T - T_\infty < 0$ in both Equation (11) and (12), which is also defined in Equation (3) as evaporative cooling occurs.

It can be concluded that the competing influence of the thermal effects in the cavitation model comes from two ways from Equation (11) as evaporative cooling occurs: (1) thermal rate of change of liquid/vapor density ratio dR/dT which is negative in Figure 1(c) together with $C_p + \sigma_\infty < 0$ and $\Delta T < 0$ as evaporation occurs, will tend to enhance the strength of m^- and (2) thermal rate of change of vapor pressure dp_v/dT which is positive in Figure 1 to suppress m^- . It is also obvious that the impacts of thermal effects will change significantly for different working temperature and pressure due to the non-linear variation of material properties from energy equation in Equation (6) and cavitation sink/source terms in Equation (10).

2.3. Turbulence Model

The k- ϵ two-equation turbulence model with a wall function treatment is presented as follows [23]:

$$\frac{\partial(\rho_m u_j k)}{\partial x_j} = P_t - \rho_m \epsilon + \frac{\partial}{\partial x_j} \left[\left(\mu_t + \frac{\mu_r}{\sigma_k} \right) \frac{\partial k}{\partial x_j} \right]\quad (13)$$

$$\frac{\partial(\rho_m u_j \epsilon)}{\partial x_j} = C_{\epsilon_1} \frac{\epsilon}{k} P_t - C_{\epsilon_2} \rho_m \frac{\epsilon^2}{k} + \frac{\partial}{\partial x_j} \left[\left(\mu_t + \frac{\mu_r}{\sigma_\epsilon} \right) \frac{\partial \epsilon}{\partial x_j} \right]\quad (14)$$

where the production term of turbulent kinetic energy (P_t) and the Reynolds stress tensor are defined as:

$$\begin{aligned}P_t &= \tau_{ij} \frac{\partial u_i}{\partial x_j}; \tau_{ij} = -\rho_m \overline{u'_i u'_j} \\ \overline{\rho_m u'_i u'_j} &= \frac{2 \rho_m k \delta_{ij}}{3} - \mu_t \left(\frac{\partial u_i}{\partial x_j} + \frac{\partial u_j}{\partial x_i} \right)\end{aligned}\quad (15)$$

with $C_{\epsilon_1} = 1.44$, $C_{\epsilon_2} = 1.92$, $\sigma_\epsilon = 1.3$, $\sigma_k = 1.0$. The turbulent eddy viscosity is defined as:

$$\mu_t = \frac{\rho_m C_\mu k^2}{\epsilon}, \quad C_\mu = 0.09\quad (16)$$

As mentioned above, a filter-based model (FBM) [24] is also adopted. This model limits the influence of the eddy viscosity based on the local numerical resolution, essentially forming a combined direct numerical simulation and RANS model. Specifically, the level of the turbulent viscosity is corrected by comparing the turbulence length scale and the filter size Δ , which is based on the local meshing spacing:

$$\mu_t = 0.09 \rho_m \frac{k^2}{\varepsilon} \min(1, \frac{\Delta \cdot \varepsilon}{k^{3/2}}) \quad (17)$$

By imposing the filter, the turbulence length scale will not be resolved if it is smaller than the filter size. The filter size is chosen to be comparable to the maximum grid size:

$$\Delta = \max(\Delta_{\text{present}}, \Delta_{\text{grid}}) \quad (18)$$

Thus if the grid resolution is significantly smaller than the turbulence length scale in the entire flow field, the solution will approach that of a direct numerical simulation; for inadequately resolved computations, the RANS model is recovered. Similar concepts can be found in studies of VLES [25,26].

2.4. Numerical method

Detailed numerical procedures for the cavitation model and associated fluid dynamics equations adopted here utilize a modified pressure-based approach for large density jump as well as thermal effects, as reported in [8,9]. The controlled variation scheme (CVS) [28] is applied to discretize the convection scheme, and central difference is used for both pressure and diffusion terms. The CVS scheme can prevent the oscillations under sharp gradients caused by the phase change while preserving second-order accuracy elsewhere.

As for the boundary conditions, liquid volume fraction, velocity, temperature and turbulent quantities are specified at the inlet. For the outlet, pressure and other flow variables are extrapolated. On the walls, pressure, liquid volume fraction, and turbulent quantities are extrapolated along with no-slip and adiabatic conditions. Additionally, the pressure at the reference point (P_∞) in the upstream is also fixed to define the cavitation number σ_∞ [8,9].

Based on the eddy-to-laminar viscosity ratio at the inlet, the inlet turbulent quantities can be given as following:

$$k = \frac{3}{2} (U_\infty I)^2, \quad \varepsilon = \frac{C_\mu k^2}{\nu_L (\mu_T / \mu_L|_{\text{inlet}})} \quad (19)$$

where I is turbulence intensity (2% for entire study), and eddy-to-laminar viscosity ratio, $\mu_T / \mu_L|_{\text{inlet}}$, is equal to 1000 in all the cases during the current study.

3. Results and Discussion

3.1. Test Geometry

We simulate flow over a 2D quarter hydrofoil in Figure 2 with the experimental measurements by Hord [29]. Since we have illustrated in Figure 1 and used Equation (11) and (12) to highlight the impacts of thermal effects will change significantly for different temperatures, we select both Case 290C and 296B to calibrate the role of model parameters and uncertainty of fluid properties. Figure 2 and Table 2 summarize the geometries, corresponding boundary conditions, and the

flow conditions of the test cases selected to aid the model validation.

Substance	Case	σ_∞	Re_∞	T_∞
Liquid nitrogen	290C	1.70	9.1×10^6	83.06K
Liquid nitrogen	296B	1.61	1.1×10^7	88.54K

Table 2. Summary of simulation setups and fluid properties

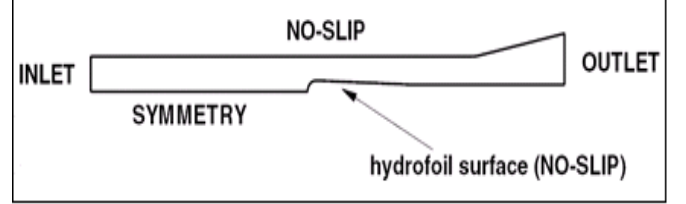


Figure 2. Schematic of the geometries and the boundary conditions of the cases considered.

3.2. Pressure and Temperature Predictions

Figure 3 compares the predicted and experimentally measured pressure and temperature profiles [29] on the hydrofoil surface with $C_{\text{dest}} = 0.68$ and $C_{\text{prod}} = 54.4$ suggested in [3]. Overall, the cavitation and turbulence models with filter (FBM) can consistently capture the main features of both pressure and thermal profiles. The temperature drop inside the cavity in Figure 3(b) and (d) also clearly demonstrates the evaporative cooling resulting from cryogenic cavitation.

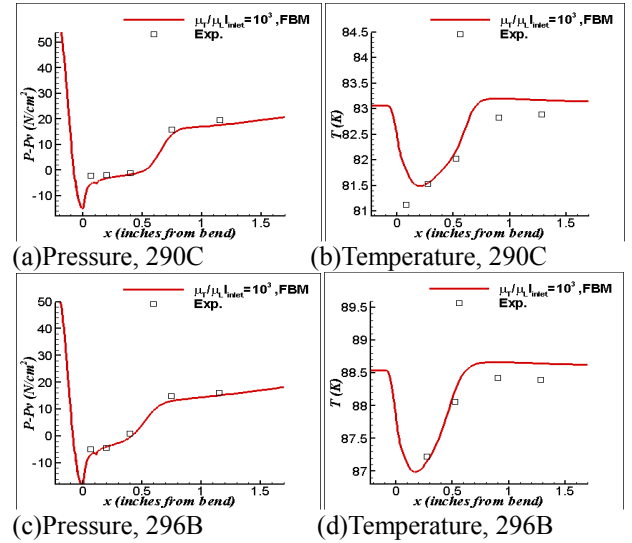


Figure 3. Pressure and temperature of cryogenic cavitation along surface.

In Figure 4, we compare the present cryogenic model solution with the isothermal solution for Case 290C, obtained by using the identical model with $C_{\text{dest}} = 0.68$ and $C_{\text{prod}} = 54.4$ except that the energy equation is not invoked. Clearly, the thermal field does affect the cavity structures. The cavity size in Figure 4(b) is reduced due to the thermal effect because the temperature drop inside the cavity in Figure 4(a) decreases the local vapor pressure and hence increases the local cavitation number (please refer to Equation (3)), resulting in a weaker

cavitation intensity and higher overall liquid volume fraction in the cavity (as shown in Figure 4(c)). Besides, the pressure inside the cavity is steeper under the cryogenic condition than that under the isothermal condition in Figure 4(d) due to the variation in thermal rate of change of vapor pressure dP_v/dT . The purpose of Figure 4 is to illustrate the thermal effects could significantly change the pressure fields and cavity structures under cryogenic conditions.

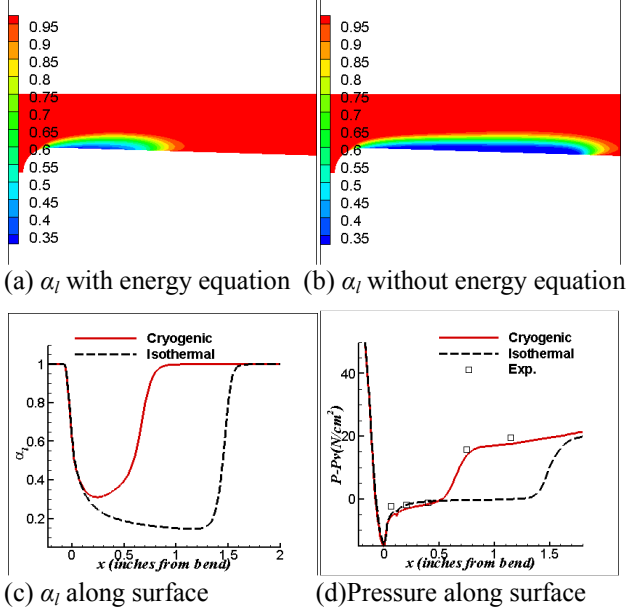


Figure 4 Comparisons for Case 290C between results with/without energy equation

3.3 Surrogates-based Global Sensitivity Assessment

Since minor changes in flow environment can lead to substantial changes in the predictions in cryogenic environment, it is imperative to appraise the role of model parameters and uncertainties in material properties on the predictions. In this section, we characterize the parameters using surrogate-based global sensitivity analysis (GSA) and then calibrate the cryogenic cavitation model parameters. We use polynomial response surface approximation (PRS, [20]), Kriging (KRG, [21]), radial basis neural network (RBNN, [22]), and a weighted average surrogate model (PWS) for approximation of response. [4,19].

We use variance-based, non-parametric GSA method, proposed [16] to evaluate the sensitivity of predictions with respect to model parameters and material properties. In this method, the objective function is decomposed into additive functions of variables and interactions among variables. This allows the total variance (V) in the objective function to be expressed as a combination of the main effect of each variable (V_i) and its interactions with other variables (V_{ij}). The sensitivity of the objective function with respect to any variable is measured by computing its sensitivity indices. The sensitivity indices of main effect (S_i) and total effect (S_i^{total}) of a variable are given as follows:

$$S_i = \frac{V_i}{V}, \quad S_i^{total} = \frac{(V_i + V_{iZ})}{V} \quad (20)$$

We choose C_{dest} , C_{prod} , ρ_v , and L as design variables, while holding the Re_∞ and σ_∞ constant for the given cases. The performance of predictions for the cryogenic cavitation models are represented by root mean square (RMS) values of the differences between computed and experimental values along hydrofoil surface for temperature (T_{diff}) and pressure (P_{diff}) as our objectives. The model parameters, C_{dest} and C_{prod} , vary from 0.578 to 0.68 and 46.2 to 54.4 respectively. The material properties ρ_v and L are perturbed within $\pm 10\%$ of the value they assume from the NIST database [5].

These two empirical constants C_{dest} and C_{prod} directly control the evaporation and condensation rate via the cavitation model. Besides, ρ_v , as a fluid property which dominates the evaporative cooling, also appears directly in cavitation sink term, and L will determine the energy absorb or release during the phase change. Therefore, these four model parameters and fluid properties are selected as our design variables.

To facilitate the development of surrogate models, 70 “training” points are selected using combined face-centered cubic composite design (FCCD, 25 points) and Latin hypercube sampling (LHS, 45 points). Five additional test points which are not included in the 70 training points are used to validate the surrogate models for both case 290C and 296B. We evaluate T_{diff} and P_{diff} for each data point using CFD simulations and construct PRS, Kriging, RBNN, and PWS models of both objectives in normalized variable space. All variables and objectives are normalized such that ‘0’ corresponds to the minimum value and ‘1’ corresponds to the maximum value. Normalized variables and objectives are denoted by a superscript ‘*’. We use second order polynomials for PRS and a spread coefficient=0.4~0.7 for RBNN. Relevant details of the quality of fit of surrogate models are documented in [4].

The smallest root mean square of PRESS (PRESS is the predicted residual sum of square) in Appendix Table A1 indicates that the KRG model has the best performance, while RBNN has the worst overall performance. The contribution of different surrogate models to the PWS model is given by the weights in Appendix Table A2. Since the performance of KRG is the best, its weight is also the greatest.

There are additional five test points to validate the surrogates. Appendix Table A3 shows the locations of these points in the normalized design space for both Case 290C and 296B. The simulation results are presented to compare with the prediction of surrogates in Appendix Table A4 and A5 for Case 290C, and Appendix Table A6 and A7 for Case 296B.

Due to the best performance in error estimate in Appendix Table A1 and tests for additional five samples from Appendix Table A4 to A7, we will use KRG to demonstrate the global sensitivity analysis. Appendix Table A8 and A9 show that the interactions among parameters are very strong for pressure since the difference between main and total sensitivity indices are obvious for Case 290C and 296B. As for temperature, Case 296B has stronger interactions than those of Case 290C.

From Figure 5 and 6 which evaluate the weights of each variables via global sensitivity analysis as pie-charts, C_{dest} and ρ_v are very important for P_{diff} , and while C_{prod} and L don’t have noticeable contribution in both cases. Besides, the weights of P_{diff} are very similar for Case 290C and 296B. As for T_{diff} , the

importance of L clearly increases, and even becomes the same important as C_{dest} and ρ_v in Case 296B, while in Case 290C, the weight is just around 6%. This indicates that the thermal effects and importance of the thermodynamics property will influence the thermal field more significantly as temperature increases (Case 296B has higher inlet temperature than Case 290C).

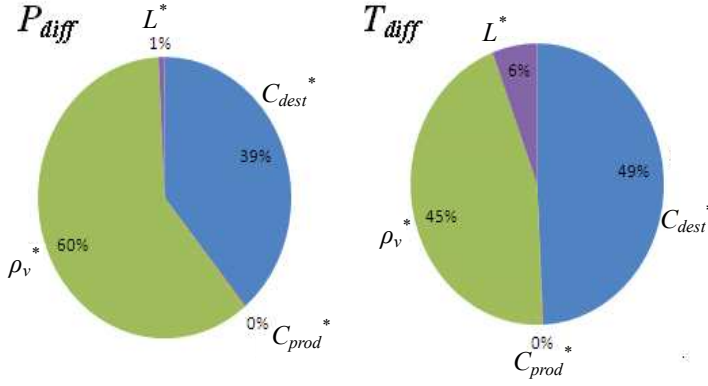


Figure 5. Pie-chart of global sensitivity analysis for Case 290C (KRG (Kriging), total indices)

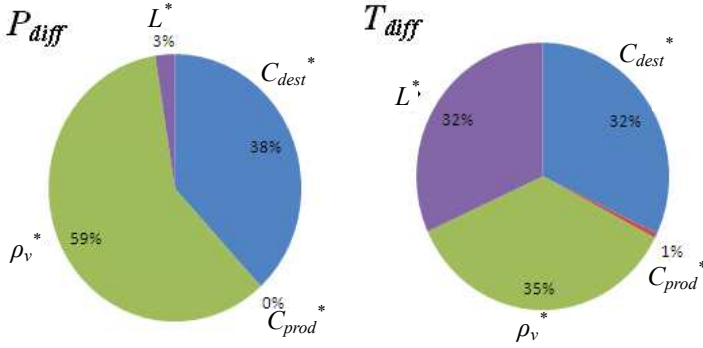


Figure 6. Pie-chart of global sensitivity analysis for Case 296B (KRG (Kriging), total indices)

C_{prod} is not important within this design space from the pie-chart, and this implies that the sensitivity of condensation term is not significant compared with evaporation term or C_{dest} . This should be because cavitation initiates from evaporation, and this behavior already decides how strong the cavitation dynamics and how low the liquid volume fraction will be inside the cavity. Besides, the condensation strength will also depend on the evaporation strength. Just imagine if we give a very low strength on evaporation term, the condensation dynamics will still be weak even C_{prod} is large. This is because the vapor inside the cavity will not be sufficient for source term. Thus the weight of C_{dest} is much more important than C_{prod} in this design space.

As we know, the cavitation terms can be expressed as following in Equation (10):

$$\dot{m}^- = \frac{C_{dest} \alpha_l \rho_l \min(0, p - p_v)}{t_\infty \rho_v (0.5 \rho_l U_\infty^2)} \quad \dot{m}^+ = \frac{C_{prod} (1 - \alpha_l) \max(0, p - p_v)}{t_\infty (0.5 \rho_l U_\infty^2)}$$

Therefore we can group $C_{dest}/t_\infty/\rho_v^*$ and C_{prod}/t_∞ together to show the variation in strength of cavitation sink and source term under the combinations of design variables, and then

normalize these values in Figure 7 and 8. This is the direct impact which indicates the direct appearance of design variables in the cavitation model. All the normalized values here are from the previous simulation results of the 70 training points.

Figure 7 and 8 show the distributions of P_{diff}^* vs. $(C_{dest}/t_\infty/\rho_v^*)^*$ are quite the same for both Case 290C and 296B. This is because both cases have consistent pie-charts and weights in the pressure prediction P_{diff}^* in Figure 5 and 6.

As, $(C_{dest}/t_\infty/\rho_v^*)^*$ is small in Figure 7 and 8, the sink term is not strong enough so that the cavity size is too small, and hence P_{diff}^* will be large. When $(C_{dest}/t_\infty/\rho_v^*)^*$ goes up to certain moderate value, the corresponding evaporation term gives a more suitable cavity size with a smaller value of P_{diff}^* . For even large values of $(C_{dest}/t_\infty/\rho_v^*)^*$, the cavity sizes will be too large, and P_{diff}^* will increase again. This clearly indicates that there exists a suitable range for sink term or C_{dest} to obtain good pressure predictions. For the same value of $(C_{dest}/t_\infty/\rho_v^*)^*$, different P_{diff}^* and T_{diff}^* can sometimes be obtained. This is because different fluid properties, namely ρ_v^* or L^* , influence the flow fields. We haven't really included this factor in Figure 7 and 8, and refer it as indirect impact.

As for $(C_{dest}/t_\infty/\rho_v^*)^*$ vs. T_{diff}^* , we still can roughly see similar trends as shown in $(C_{dest}/t_\infty/\rho_v^*)^*$ vs. P_{diff}^* , but the distributions are not so consistent for both Case 290C in Figure 7 and 296B in Figure 8. Again, this is due to different pie-charts of T_{diff}^* for both cases as shown in Figure 5 and 6. This also implies different impacts of thermal effects at different temperatures which we have already stated before.

For ρ_v^* , besides direct appearance in the sink term, it is also part of fluid property. As a fluid property, it can change the value of mixture density to exhibit different evaporative cooling inside the cavity, and hence affects the cavity size and cavitation dynamics. Therefore, it owns both direct and indirect impacts, and we can see its weight of P_{diff}^* from global sensitivity analysis is even larger than C_{dest} in Figure 5 and 6.

As for $(C_{prod}/t_\infty)^*$, there is really no trend for P_{diff}^* and T_{diff}^* . This is because from the pie-chart in Figure 5 and 6, we can see the importance of C_{prod} is insignificant, and all these distributions in Figure 7 and 8 would be mainly due to the contributions of sink term. Therefore the random distributions for $(C_{prod}/t_\infty)^*$ vs. P_{diff}^* and T_{diff}^* in Figure 7 and 8 help us validate the insignificant weight of C_{prod} in Figure 5 and 6 from another viewpoint.

3.4 Optimization of Model Parameters

In the previous section, we observed that one of the model parameters C_{dest} significantly influences the performance of the present cryogenic cavitation model. Therefore we fix another model parameter C_{prod} at 54.4 which is not really influential on predictions, and assume the temperature-dependent material properties ρ_v and L obtained from the NIST database [5] to be correct. Then we allow the model parameter C_{dest} to vary between 0.578 and 0.68, and try to find the optimization values which give P_{diff} and T_{diff} as low as possible. There are 11 training points within the design space with equal spacing. From the simulations shown in Figure 9, we can see for Case 290C, the trends of these two objectives are almost opposite, and for Case 296B, these two objectives are of the same trends.

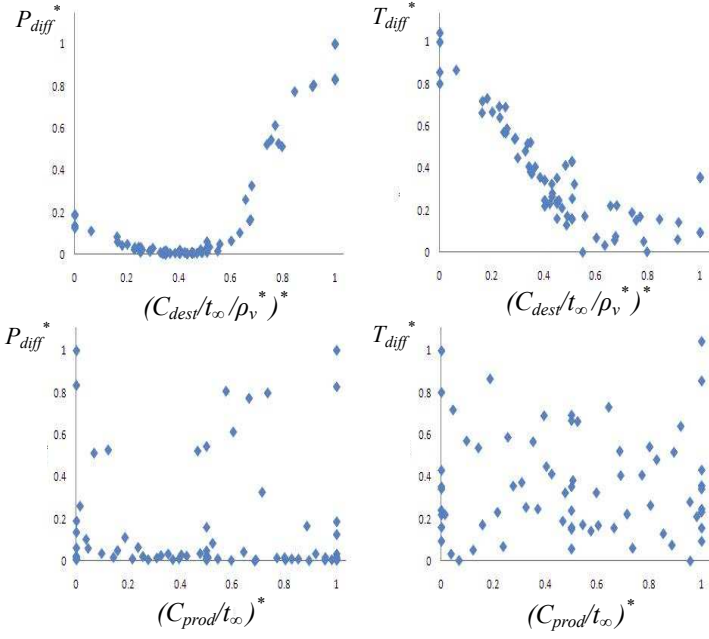


Figure 7. Illustration of the direct impact of Case 290C.

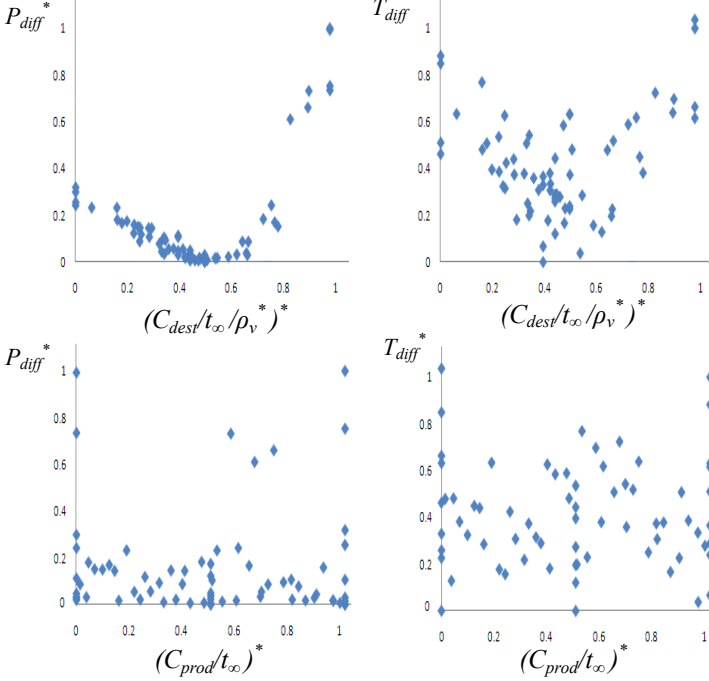
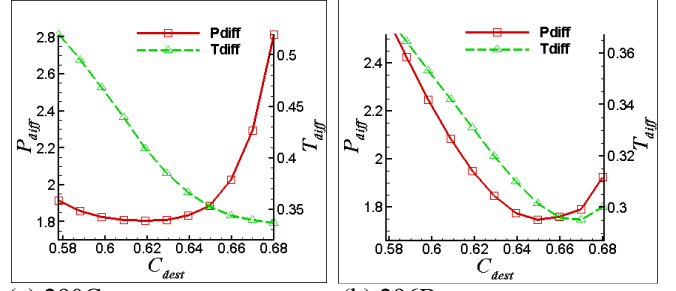


Figure 8. Illustration of the direct impact of Case 296B.

To represent the responses P_{diff} and T_{diff} using surrogate models, we sample data using CFD simulations from Figure 9. P_{diff} and T_{diff} estimated by surrogate models shown in Figure 10(a) and 11(a) clearly exhibit the same trend as simulations in Figure 9. As before, we construct PRS, KRG, RBNN, and PWS models. The error estimates and the weights associated with different surrogates in PWS model are summarized in Table A10 and A11. Besides PRS for P_{diff} in Case 290C, all the surrogates yield a good accuracy.

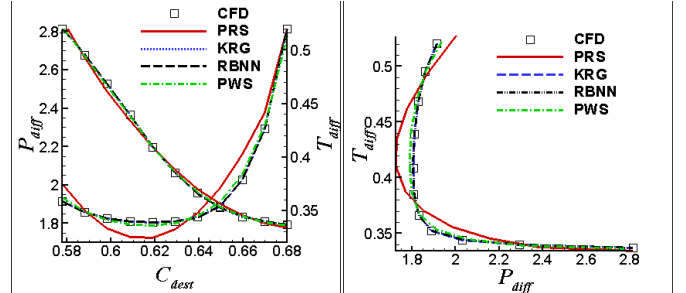


(a) 290C

(b) 296B

Figure 9. Location of points (C_{dest}) and corresponding responses (P_{diff} is shown on left y-axis, and T_{diff} is shown on right y-axis) used for calibration of the cryogenic cavitation model.

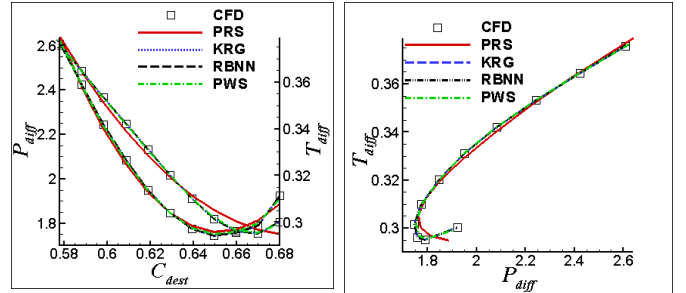
The function space and the variable space illustration of Pareto optimal front (POF) obtained through different surrogate models are shown in Figure 10 and 11. We observe that different POFs obtained by using multiple surrogate models are close to one another in both function and variable spaces (Besides PRS for P_{diff} in Case 290C). We note that the pressure fluctuations play a more important role in determining the cavitation dynamics and the loadings on fluid machinery. Consequently, more accurate pressure prediction is our primary objective. We select a solution on the POF for validation, such that notable reduction in P_{diff} can be realized without incurring significant deterioration of T_{diff} . Therefore the optimal C_{dest} will be 0.65 from Figure 10 and 11. It also indicates that different thermal effects will not significantly affect the choice of optimal C_{dest} .



(a) Variable space

(b) Function space

Figure 10. Pareto optimal front and corresponding optimal points for Case 290C.



(a) Variable space

(b) Function space

Figure 11. Pareto optimal front and corresponding optimal points for Case 290C.

(KRG, Kriging; PRS, Polynomial Response Surface; RBNN, Radio Basis Neural Network; PWS, PRESS-Based Weighted Average Surrogate.)

3.5 Optimization for Liquid hydrogen

We have repeated similar model calibration process for liquid nitrogen by considering Case 249D ($\sigma_\infty=1.57$, $T_\infty=20.7\text{K}$, $Re_\infty=2\times 10^7$) and 255C ($\sigma_\infty=1.49$, $T_\infty=22.2\text{K}$, $Re_\infty=2.5\times 10^7$), the optimal value of C_{dest} will be 0.78.

3.6 Improvement by Filter-based Turbulence Model

Compared with Goel. et al [4], our current results exhibit improvement in both pressure and temperature prediction by utilizing filter-based model (FBM, [24]). This model helps us reduce the uncertainties from inlet turbulent quantities. The improvement is summarized in Table 3. Please note that our C_{dest} is 0.65 for liquid nitrogen and 0.78 for liquid hydrogen, while Goel. et al use 0.639 and 0.767 respectively.

Case	Fluid	P_{diff}		T_{diff}	
		Current results	Goel et al [4]	Current results	Goel et al [4]
290C	Nitrogen	1.888	2.012	0.352	0.466
296B	Nitrogen	1.745	3.491	0.301	0.413
249D	Hydrogen	1.900	1.928	0.310	0.421
255C	Hydrogen	2.390	2.890	0.549	0.614

Table 3. Performance comparisons between current study and Goel. et al [4].

We have also used $C_{dest}=0.65$ to other liquid nitrogen cases listed in the experiment [29], and the simulation results are also very consistent to experimental data in Table 4. This exercise helps us to validate our model parameters are also suitable for other cases.

Case	σ_∞	T_∞ (K)	P_{diff}	T_{diff}
283B	1.73	77.65	1.66	0.32
283C	1.80	77.71	1.31	0.19
293A	1.75	77.64	2.23	0.39

Table 4. $C_{dest}=0.65$ for other liquid nitrogen cases.

4. Conclusions

In this study, we choose C_{dest} , C_{prod} , ρ_v , and L as design variables and use different surrogate models, PRS, KRG, RBNN, and PWS, to construct the response of pressure prediction P_{diff} and temperature prediction T_{diff} for cryogenic cavitation. As documented in our previous study [27], the inlet conditions of the turbulence model can critically affect the outcome of cavitation structure. The filter-based model can help significantly reduce the uncertainty in this regard. We have re-examined the surrogate-based cryogenic modeling efforts previously reported by Goel et al. [4] based on a more refined turbulence approach to better probe the combined turbulent cavitating flow predictive capabilities.

It is found that the performance of the current cavitation model is affected more by model parameter C_{dest} associated with the evaporation term and the fluid property ρ_v which controls the evaporative cooling. The condensation term (C_{prod}) is not important at all within this design space, and latent heat L becomes significant only in temperature prediction.

We have also observed that there is a range of evaporation term or C_{dest} which can give better accuracy of pressure prediction. We recommend $C_{dest}=0.65$ and 0.78 for liquid nitrogen and hydrogen respectively, and C_{prod} is 54.4 for both fluids.

5. Acknowledgments

The present efforts have been supported by NASA Constellation University Institute Program (CUIP).

6. Appendix

Acronyms in this appendix:

PRS	Polynomial Response Surface [20]
KRG	Kriging [21]
RBNN	Radio Basis Neural Network [22]
PWS	PRESS-Based Weighted Average Surrogate [4,17,19]
PRESS	The predicted residual sum of square
R^2_{adj}	Coefficient of multiple determination [20] (better fit as it is closer to 1)

Surrogate	P_{diff}^*		T_{diff}^*	
	290C	296B	290C	296B
PRESS _{rms} of PRS	6.38%	11.90%	9.11%	10.02%
R^2_{adj} of PRS	0.962	0.939	0.892	0.928
PRESS _{rms} of KRG	2.97%	2.93%	2.48%	6.62%
PRESS _{rms} of RBNN	13.91%	11.67%	13.31%	19.03%
PRESS _{rms} of PWS	3.97%	5.44%	5.50%	9.20%

Table A1 Error estimate for different cases and surrogates (70 training points)

Surrogate	P_{diff}^*		T_{diff}^*	
	290C	296B	290C	296B
PRS	44.2%	27.5%	31.8%	36.4%
KRG	47.4%	44.5%	45.0%	39.6%
RBNN	8.4%	28.3%	23.2%	24.0%

Table A2 Weights associated with different surrogate models (70 training points)

	C_{dest}^*	C_{prod}^*	ρ_v^*	L^*
No.1	0.692	0.2336	0.7828	0.6928
No.2	0.5806	0.9394	0.2	0.7639
No.3	0.8039	0.1432	0.4183	0.8426
No.4	0.0435	0.4289	0.0991	0.4591
No.5	0.3308	0.6054	0.8575	0.0395

Table A3. Test points inside the normalized design space

PRS	KRG	RBNN	PWS	CFD
-2.3%	-2.7%	-8.0%	-3.6%	1.865
-7.4%	-2.7%	-5.4%	-5.0%	3.788
30.6%	3.0%	12.0%	14.8%	2.387
19.2%	-5.3%	-1.6%	4.3%	1.847
-5.7%	0.2%	-3.7%	-2.7%	1.969

Table A4. Predictions error of P_{diff} for case 290C

PRS	KRG	RBNN	PWS	CFD
-0.2%	-0.5%	1.2%	0.0%	0.406
1.4%	-1.7%	-9.1%	-2.4%	0.341
6.4%	1.8%	-0.7%	2.7%	0.321
3.2%	-1.1%	1.1%	0.8%	0.406
-4.4%	0.1%	-0.2%	-1.4%	0.538

Table A5. Predictions error of T_{diff} for case 290C

PRS	KRG	RBNN	PWS	CFD
-15.9%	-5.1%	12.2%	2.8%	2.3231
55.0%	-3.6%	46.3%	-20.9%	1.9201
35.7%	-6.6%	-26.0%	0.4%	1.9439
0.0%	-6.8%	28.1%	-4.6%	1.7866
-12.0%	-4.6%	28.8%	-2.7%	2.6871

Table A6. Predictions error of P_{diff} for case 296B

PRS	KRG	RBNN	PWS	CFD
0.6%	0.3%	-2.2%	0.2%	0.2979
6.1%	6.4%	1.5%	-4.9%	0.3046
8.5%	6.7%	0.2%	-5.5%	0.2768
1.2%	0.9%	-1.6%	-0.4%	0.3467
-0.6%	1.0%	-1.3%	0.1%	0.3915

Table A7. Predictions error of T_{diff} for case 296B
(The column for CFD in Appendix Table A4 to A7 denotes simulation results before normalized.)

	C_{dest}^*	C_{prod}^*	ρ_v^*	L^*
P_{diff}^*	0.176/0.531	5E-5/0.002	0.461/0.819	0.002/0.010
T_{diff}^*	0.456/0.532	1E-4/0.001	0.405/0.485	0.058/0.062

Table A8. Global sensitivity for 290C with KRG
(main/total effect)

	C_{dest}^*	C_{prod}^*	ρ_v^*	L^*
P_{diff}^*	0.035/0.612	2E-4/0.001	0.360/0.954	0.000/0.040
T_{diff}^*	0.137/0.407	0.006/0.008	0.182/0.453	0.403/0.404

Table A9. Global sensitivity for 296B with KRG
(main/total effect)

	P_{diff}^*		T_{diff}^*	
Surrogate	290C	296B	290C	296B
PRESS _{rms} of PRS	16.01%	4.46%	3.82%	6.00%
R ² _{adj} of PRS	0.900	0.994	0.994	0.997
PRESS _{rms} of KRG	7.01%	4.87%	1.89%	1.91%
PRESS _{rms} of RBNN	4.00%	6.74%	1.56%	0.73%
PRESS _{rms} of PWS	7.45%	5.10%	3.20%	1.83%

Table A10 Error estimate for different cases and surrogates
(11 training points)

	P_{diff}^*		T_{diff}^*	
Surrogate	290C	296B	290C	296B
PRS	20.8%	35.8%	23.6%	13.5%
KRG	36.9%	34.5%	37.1%	39.5%
RBNN	42.3%	29.6%	39.3%	47.0%

Table A11 Weights associated with different surrogate models
(11 training points)

7. Nomenclature

σ_∞	Free stream cavitation number
σ	Cavitation number based on the local temperature
$C_{\varepsilon 1}, C_{\varepsilon 2}$	Coefficients of k- ε turbulence model
$\sigma_\varepsilon, \sigma_k$	Coefficients of k- ε turbulence model
C_p	Pressure coefficient
D	Characteristic length scale
f_v	Vapor mass fraction
h	Enthalpy
I	Turbulence intensity
K	Turbulent kinetic energy
L	Latent heat
m^+, m^-	Source and sink terms in the cavitation model
P_{diff}	L ₂ norm between experiment and predicted pressure
Pr	Prandtl number
Pt	Production term of turbulent kinetic energy
P_v	Saturation vapor pressure
Re	Reynolds number
S	Sensitivity indices
T	Temperature
T_{diff}	L ₂ norm between experiment and predicted temperature
t_∞	Reference time scale, $t_\infty = D/U_\infty$
U_∞	Reference velocity
u	Velocity
x	Space variable
V	total variance
α_l	Liquid volume fraction
ρ	Density
μ	Dynamic viscosity
$\mu_T/\mu_L _{inlet}$	Eddy-to-laminar viscosity ratio at the inlet
Φ_m	Mixture property
ε	Turbulent dissipation rate
Δ	Filter size in filter-based model
Subscript	
ij	Interaction component
j	Component
l	Liquid
L	Laminar
m	Mixture property
T	Turbulent
v	Vapor
ω	Free stream quantities
Superscript	
$*$	Normalize value
total	Total effect

8. References

- [1]Knapp RT Daily JW, Hammitt FG. 1970, *Cavitation*. McGraw-Hill, New York.
- [2]Brennen CE. 1995, *Cavitation and Bubble Dynamics*, Oxford University Press, New York.
- [3]Utturkar Y, Wu J, Wang G, Shyy W. 2005, "Recent Progress in Modeling of Cryogenic Cavitation for Liquid Rocket Propulsion," *Progress in Aerospace Sciences*, 41(7), 558-608
- [4]Goel T, Zhao J, Thakur S, Haftka RT, Shyy W, Zhao J. 2008, "Surrogate Model Based Strategy for Cryogenic Cavitation Model Validation and Sensitivity Evaluation," *Int. J. Numer. Meth. Fluids*, 58, 969-1007.
- [5]Lemmon EW, McLinden M.O, Huber M.L. REFPROP: 2002, Reference Fluid Thermodynamic and Transport Properties, *NIST Standard Database 23, version 7.0*.
- [6]Chen Y, Hesiter SD. 1994, "A Numerical Treatment for Attached Cavitation," *J Fluids Eng*, 116, 613-618.
- [7]Deshpande M, Feng J, Merkle CL. 1997, "Numerical Modeling of the Thermodynamic Effects of Cavitation," *J. Fluids Eng*, 119, 420-427.
- [8]Senocak I, Shyy W. 2004, "Interfacial Dynamics-Based Modeling of Turbulent Cavitating Flows, Part-1: Model Development and Steady-State Computations," *Int. J. Numer. Meth. Fluids*, 44, 975-995.
- [9]Senocak I, Shyy W. 2004, "Interfacial Dynamics-Based Modeling of Turbulent Cavitating Flows, Part-2: Time-Dependent Computations," *Int. J. Numer. Meth. Fluids*, 44, 997-1016.
- [10]Merkle CL, Feng J, Buelow PEO. 1998, "Computational Modeling of Sheet Cavitation," *Proc. 3rd International Symposium on Cavitation*, Grenoble, France.
- [11]Singhal Ak, Li H, Athavale MM, Jiang Y. 2001, "Mathematical Basis and Validation of the Full Cavitation Model," *ASME Paper FEDSM2001-18015*.
- [12] Kunz RF, Boger DA, stinebring DR, Chyczewski TS, Lindau JW, Gibeling HJ, Venkateswaran S, Govindan TR. 2000, "A preconditioned Navier –stokes method for two phase flows with application to cavitation prediction," *Comput. Fluids*, 29, 849-875.
- [13]Hosangadi A, Ahuja V. 2006, "A Numerical of Cavitation in Cryogenic Fluids Part II; New Unsteady Model for Dense Cloud," *Cavitation. 6th International Symposium on Cavitation*, Wageningen, Netherlands.
- [14]Aliabadi S, Tu SZ, Watts MD. 2005, "Simulation of Hydrodynamic Cavitating Flows Using Stabilized Finite Element Method," *43th AIAA Aerospace Science Meeting and Exhibit*, Reno, Nevada.
- [15]Giorgi MGD, Ficarella A, Chiara F, Laforgia D. 2005, "Experimental and Numerical Investigations of Cavitating Flows," *35th AIAA Fluids Dynamics Conference and Exhibit*, Toronto, Ontario Canada.
- [16]Sobol, IM, 1993, "Sensitivity Analysis for Nonlinear Mathematical Models," *Mathematical Modeling & Computational Experiment* 1(4), 407.
- [17]Queipo, NV, Haftka, RT, Shyy, W, Goel, T, Vaidyanathan, R, and Tucker, PK, 2005, "Surrogate Based Analysis and Optimization," *Progress in Aerospace Sciences*, 41, 1-28.
- [18]Li, W, Padula, S. 2004, "Approximation Methods for Conceptual Design of Complex Systems", *Proceedings of 11th International Conference on Approximation Theory*, (eds. Chui C, Neaumtu M, Schumaker L).
- [19]Goel, T, Haftka, RT, Shyy, W, Queipo, NV, 2006, "Ensemble of Multiple Surrogates", accepted for publication in *Structural and Multidisciplinary Optimization*.
- [20]Myers, RH, Montgomery, DC, 1995, *Response Surface Methodology*, John Wiley, Sons, Inc.
- [21]Matheron, G, 1963, "Principles of Geostatistics," *Economic Geology*, 58, 1246-1266.
- [22]Orr, MJL, 1996, *Introduction to Radial Basis Function Networks*, *Center for Cognitive Science*, Edinburgh University, EH 9LW, Scotland, UK. <http://www.anc.ed.ac.uk/~mjo/rbf.html>
- [21]Matheron, G, 1963, "Principles of Geostatistics", *Economic Geology*, 58, 1246-1266.
- [22]Orr, MJL, 1996, *Introduction to Radial Basis Function Networks*, *Center for Cognitive Science*, Edinburgh University, EH 9LW, Scotland, UK. <http://www.anc.ed.ac.uk/~mjo/rbf.html>.
- [23]Lauder BE, Spalding DB, 1974, "The Numerical Computation of Turbulent Flow," *Comp. Meth. Appl. Mech. Eng*, 3, 269-289.
- [24]Wu JY, Shyy W, 2004, "Filter Based Unsteady RANS Computational," *International Journal of Heat and Fluid Flow*, 25, 10-21.
- [25]Ruprecht A, Helmrich T, Buntic I. 2005, "Very Large Eddy Simulation for the Prediction of Unsteady Vortex Motion," *Conference on Modeling Fluid Flow (CMFF'05), The 12th International Conference on Fluid Flow Technologies*. Budapest, Hungary.
- [26]Liu NS, Shih TS, 2006, "Turbulence Modeling for Very Large-Eddy Simulation," *AIAA J.*, 44(4), 687-697.
- [27] Tseng C and Shyy W., 2009, "Turbulence Modeling for Isothermal and Cryogenic Cavitation", *AIAA Paper No. 2009-1150*. In 47th AIAA Aerospace Science Meeting, Orlando, FL
- [28]Shyy W, Thakur SS, Ouyang H, Liu J, Bloesch E. , 2007, *Computational Techniques for Complex Transport Phenomenon*. Cambridge University Press, New York.
- [29]Hord J, 1973, *Cavitation in Liquid Cryogenics II-Hydrofoil*. NASA CR-2156.